Four-membered N-heterocyclic carbenes in carbene metal amide emitters: a quantum chemical view

Jasper Guhl, Tu Viet Chu, Tobias Kretschmer, Leonard Karl, Christian Ganter, Christel M Marian

Four-membered N-heterocyclic carbenes in carbene metal amide emitters: a quantum chemical view

Methods and Applications in Fluorescence

OPEN ACCESS

RECEIVED
10 October 2025

REVISED
13 January 2026

ACCEPTED FOR PUBLICATION
5 February 2026

PUBLISHED
24 February 2026

PAPER

Four-membered N-heterocyclic carbenes in carbene metal amide emitters: a quantum chemical view

Jasper Guhl[1], **Tu Viet Chu**[1], **Tobias Kretschmer**[1], **Leonard Karl**[2], **Christian Ganter**[2,*] and **Christel M Marian**[1,*]

[1] Institute of Theoretical and Computational Chemistry, Faculty of Mathematics and Natural Sciences, Heinrich Heine University Düsseldorf, 40204, Düsseldorf, Germany
[2] Institute of Inorganic Chemistry, Faculty of Mathematics and Natural Sciences, Heinrich Heine University Düsseldorf, 40204, Düsseldorf, Germany
[*] Authors to whom any correspondence should be addressed.

E-mail: Christian.Ganter@hhu.de **and** Christel.Marian@hhu.de

Keywords: computational molecular design, structure-property relationships, linear coinage metal complex, lactam-based carbenes, intersystem crossing, thermally activated delayed fluorescence (TADF)

Supplementary material for this article is available online

Abstract

Using computational chemistry, we have scanned a set of four-membered N-heterocyclic carbenes with bulky substituents for their ability to form carbene metal amides (CMAs) with excellent thermally activated delayed fluorescence (TADF) properties. In comparison to the properties of their well-known five- and six-membered analogs, the transition dipole moments of the first excited singlet states of the corresponding $Cu^{(I)}$ carbazolide (Cz) complexes increase. For CMAs of the most promising four-membered carbene, a lactam-based carbene (4LAC), detailed investigations of the TADF properties have been performed using advanced quantum chemical methods. Due to the small energy separation between its singlet and triplet ligand-to-ligand charge-transfer (LLCT) states, 4LAC–$Ag^{(I)}$–Cz exhibits the best ratio between reverse intersystem crossing (rISC) and intersystem crossing in the coinage metal triad for a coplanar orientation of the ligands. The TADF properties of the corresponding $Cu^{(I)}$ and $Au^{(I)}$ complexes benefit from twisted ligand–ligand alignments, achieved by using tetrafluorocarbazolide (4FCz) as donor ligand. The moderate reduction of the fluorescence rate constant upon twisting by about 45–50° is overcompensated by a decrease of the singlet–triplet energy gap, thus improving the TADF performance. Overall, with fluorescence rate constants of the order of 10^7 s^{-1} and rISC rate constants between 10^9 and 10^{10} s^{-1}, TADF should have competitive advantage over common triplet deactivation processes such as triplet–triplet annihilation. Like in other CMAs, full excited-state geometry relaxation in liquid solution is detrimental for the emission properties. In the solid state, where the formation of a perpendicular ligand–ligand alignment is sterically hindered by the environment, 4LAC–M–Cz and 4LAC–M–4FCz are predicted to be efficient TADF compounds with red to orange emission.

1. Introduction

Two-coordinate carbene metal amide (CMA) complexes, where M includes the coinage metal ions $Cu^{(I)}$, $Ag^{(I)}$ and $Au^{(I)}$ and where the amide ligand typically is a carbazolide (Cz) derivative, represent some of the most promising metal organic compounds to be used as thermally activated delayed fluorescence (TADF) emitters in organic light emitting diodes (OLEDs). By employing cyclic (alkyl)(amino)carbenes (CAACs) [1–11], bicyclic (alkyl)(amino) carbenes (BICs) [5], cyclic (amino) (barrelene) carbenes (CABCs) [12], cyclic (aryl)(amino) carbenes (CAArCs) [8, 13], monoamido-aminocarbenes (MACs) or diamidocarbenes (DACs) [3, 9, 14] in addition to conventional N-heterocyclic carbenes (NHCs) [9, 15, 16], the luminescence properties of the CMAs can be tuned across the visible light spectrum, with some exhibiting quantum yields close to unity. The recent report of two novel four-membered carbenes [17, 18], one of

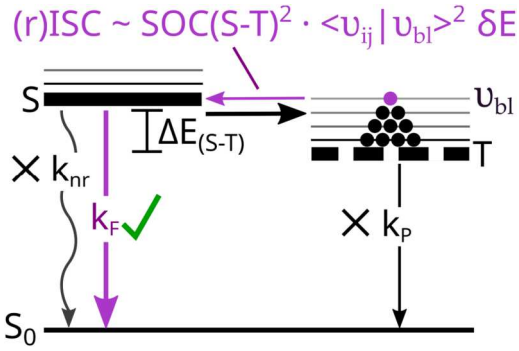

Figure 1. Schematic representation of an efficient TADF emitter. Recombination of charge carriers in an OLED populates the excited singlet and triplet states of the emitter with a ratio of 1:3. A small singlet–triplet energy gap ΔE_{ST} facilitates the thermal population of the excited singlet state via rISC from the triplet state. Ideally, the mutual electronic SOC of the excited singlet and triplet states and the Franck–Condon weighted density of vibrational states are sufficiently large to enable fast equilibration of the singlet and triplet populations. High total (prompt plus delayed) fluorescence quantum yields can be achieved if the fluorescence rate constant k_F exceeds the rate constants of competing nonradiative decay processes (k_{nr}) and of phosphorescence (k_P).

them lactam-based, sparked our interest in their performance in CMA complexes.

Due to the electron-rich Cz ligand, CMA complexes are strongly polar in the electronic ground state and typically feature ligand-to-ligand charge-transfer (LLCT) states as the lowest excited singlet and triplet states. These LLCT states exhibit smaller singlet–triplet energetic splittings ΔE_{ST} and lower phosphorescence rates than metal-to-ligand charge-transfer (MLCT) states but maintain sufficient spin–orbit coupling (SOC) strength to enable intersystem crossing (ISC) transitions [19]. The T_{LLCT} states of CMAs are therefore apt to undergo reverse intersystem crossing (rISC) to their nearby S_{LLCT} congeners, a necessary precondition for efficient TADF (figure 1).

Theoretical investigations show that the optoelectronic properties of the linear CMAs critically depend on the ligand–ligand twist and tilting angles [20–24]. Fluorescence occurs preferentially in coplanar orientations of the carbene and Cz ligands whereas radiative rate constants are close to zero in perpendicular orientations. Here, ΔE_{ST} is smallest and thermal activation of the triplet population is easy, provided that the mutual S_1–T_1 spin–orbit coupling matrix element (SOCME) is sufficiently large. Like twisting, tilting the Cz ligand appears to reduce the singlet–triplet gap and to enhance the rISC process. On the downside, large-amplitude motions in twisting and tilting coordinates are suspected to cause rapid nonradiative deactivation of the complexes [24].

In this work, we explore carbene metal amides (CMAs) composed of a four-membered carbene of N-heterocyclic carbene (NHC), monoamido-aminocarbene (MAC), cyclic (alkyl)(amino)carbene (CAAC), or lactam-based carbene (LAC) type, a coinage metal ($Cu^{(I)}$, $Ag^{(I)}$ or $Au^{(I)}$) and the electron-rich 9H-carbazol-9-yl (Cz) by means of quantum chemical methods and compare their properties to those of CMAs featuring well-known five- and six-membered carbenes. The N-heterocyclic carbenes carry diisopropylphenyl (Dipp) groups at the nitrogen atoms, CAACs and LACs are spiro-fused to a bulky substituent at the alkyl position adjacent to the carbene site. For the complexes of the most promising four-membered carbene, 4LAC, we perform detailed quantum chemical investigations of their TADF properties and compare them to those of related compounds featuring a five-membered carbene. To study the effect of the ligand–ligand twist angle on the TADF properties, in addition to Cz, 1,8-dimethyl-9H-carbazol-9-yl (2MeCz) and 1,3,6,8-tetrafluoro-9H-carbazol-9-yl (4FCz) are considered as donors.

2. Method

All calculations were performed for molecules placed in a solvent excluded surface cavity and surrounded by a polarizeable continuum model (PCM) of dichloromethane (DCM) solvent [25–27]. Minimum nuclear arrangemens were optimized by means of Gaussian 16 [28] in conjunction with the PBE0 density functional [29, 30]. Herein, def2-SV(P) basis sets [31] were employed for all ligand atoms. Small-core scalar relativistic Wood-Boring effective core potentials (ECPs) and associated TZVP valence basis sets were used for representing silver (ecp-28-mwb) and gold (ecp-60-mwb) [32]. For copper, we employed the cc-pVDZ-PP basis set [33] together with the Stuttgart-Koeln ECP [34]. Excited-state geometries were optimized with time-dependent density functional theory (TDDFT) [35, 36]. To avoid triplet instabilities, the Tamm-Dancoff approximation (TDA) [37] was used for locating the triplet equilibrium geometries. All stationary points were verfied as minima employing the analytical Hessian routines of Gaussian 16.

Bond properties of the carbenes or their complexes were analyzed with the NBO 3.0 program [38]. The natural bond order (NBO) analysis is based on an optimal transformation of a given wavefunction into a localized form, encompassing one-center (lone-pair) and two-center (bond) terms Deviations from an idealized Lewis-structure can be interpreted as electron donation from an occupied NBO orbital into a vacant NBO orbital, and their second-order interaction as backbonding. The backbonding strength (BBS) in the examined systems was calculated according to [38]

$$\mathrm{BBS} = q_i \frac{F(i,j)^2}{\epsilon_j - \epsilon_i} \qquad (1)$$

P where q_i is the donor orbital occupancy, ϵ_i and ϵ_j are the NBO orbital energies (diagonal elements) and $F(i, j)$ is the offdiagonal NBO Fock matrix element.

Energies and transition dipole moments of the singlet and triplet states were determined by means of the DFT/MRCI method [39, 40]. This semi-empirical method combines elements of density funcional theory (DFT) and multireference configuration interaction (MRCI) to compute correlated wave functions. To avoid double counting of correlation energy, the method makes use of extensive configuration selection and introduces in total 5 scaling parameters for two-electron interactions. Here, we employ the R2022 Hamiltonian, parameterized for a configuration selection threshold of 0.8 E_h and computed the first ten excited singlet and triplet states. As one-particle basis for generating the MRCI space, ground-state BH-LYP [41, 42] Kohn–Sham molecular orbitals (MOs) are used. The MOs and resolution-of-the-identity (RI)-approximated integrals [43] were determined with the Turbomole [44] program package. In these calculations, solvent–solute interactions were modeled by point charges, imported from preceding Gaussian calculations. Descriptors derived from one-particle transition density matrices of the DFT/MRCI wave functions by means of TheoDORE analyses [45] assisted in characterizing the properties of the CMAs in the excited states. MOs, difference densities and molecular structures were visualized with jmol [46].

Spin–orbit coupling (SOC) matrix elements of the DFT/MRCI wave functions were computed with the SPOCK package [47–49] employing atomic mean-field integrals [50] for all light elements and SOC-ECPs [32, 34] for the metal centers. These matrix elements are subsequently used to determine temperature dependent intersystem crossing (ISC) and reverse intersystem crossing (rISC) rate constants in harmonic oscillator and Franck–Condon (FC) approximation including Duschinsky effects. In the VIBES program [51–53], the FC-weighted density of final vibrational states is determined for a temperature-dependent Boltzmann distribution of initial vibrational states using a time correlation function approach. To determine radiative rate constants from spin–orbit mixed wavefunctions according to the Einstein formula for spontaneous emission, we carried out multi-reference spin–orbit coupling configuration interaction (DFT/MRSOCI) [54] calculations for five roots. Fluorescence rate constants k_F were calculated at the optimized geometry of the adiabatically lowest excited singlet state, component-averaged phosphorescence rate constant k_P at the optimized geometry of the first excited triplet state.

3. Results and discussion

3.1. Properties of the free carbenes

To create a solid basis for a comparison of the carbene properties, we first examined four series of four-, five- and six-membered free carbenes comprising NHCs, MACs, CAACs and LACs (figure 2, left). To complete the series, 5- and 6-membered DACs (figure 2, right) were studied as well. In our analysis, the energy of the doubly occupied σ lone-pair orbital, $\epsilon(\sigma)$ is considered an indicator of the donor capability of the carbene while the energy of the lowest unoccupied carbene π^* orbital, $\epsilon(\pi^*)$, serves as an indicator of its acceptor strength. With increasing ring size, the donor capabilities improve, whereas, with exception of the LACs, the acceptor capabilities worsen.

Comparing NHCs with CAACs (table S1) it is seen that a second nitrogen atom in the carbene heterocycle lowers $\epsilon(\sigma)$ and increases $\epsilon(\pi^*)$. Independent of the ring size, we therefore expect that the CAACs have better σ-donating and π-accepting properties than the corresponding NHCs.

Due to its strong electron-withdrawing inductive effect, the carbonyl functionality in the backbone of the MACs, LACs and DACs substantially stabilizes the σ lone-pair und thus reduces the σ donating properties of the carbene. The effect is most pronounced in the four-membered carbenes, where the carbonyl moiety is bound to both nitrogen atoms. In the five- and six-membered carbenes, the two symmetrically positioned carbonyl groups of the DACs achieve a similar stabilizing effect on the σ lone pair. The impact of the C=O group on the energy of the empty π^* orbital is even larger. Interestingly, $\epsilon(\pi^*)$ is nearly constant within the series 4LAC, 5LAC and 6LAC In contrast, the acceptor orbital of 4MAC has much lower energy than its 5MAC and 6MAC congeners. All in all, we expect the MACs, LACs and DACs to be strong acceptor carbenes featuring low-lying LLCT states when combined with a coinage metal and a strong electron-donating ligand such as Cz. With regard to their buried volumes, the carbenes follow the expected trend (table S1).

Due to their high steric demand, the six-membered CAACs and LACs with spiro-fused adamantane (Ad) residues do not form copper complexes with nearly coplanar carbene-Cz orientation (table 1). To get an idea, how strongly the residue influences the carbene properties, we carried out calculations for 6CAAC(Me) and 6LAC(Me) which carry two methyl groups instead of Ad. As exptected, the replacement reduces the buried volume of the carbene. Electronically, we observe slightly reduced donor properties in the methyl-substituted compounds while the acceptor properties remain unchanged compared to 6CAAC(Ad) and 6LAC(Ad), respectively.

3.2. Properties of the carbene copper carbazolides

The primary objective of this section is to estimate the TADF properties of carbene–Cu–Cz complexes based on the results of cost-effective calculations. In particular, we want to assess the potential of CMAs carrying novel carbene substituents (4NHC, 4MAC, 4CAAC, mLAC with m = 4,5,6) in comparison to well-known five- and six-membered CAAC, MAC

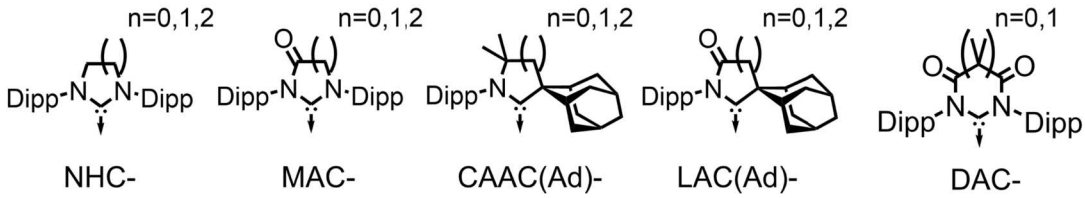

Figure 2. Carbenes scanned in this work for their donor and acceptor properties and their steric demand.

Table 1. Properties of the carbene–Cu–Cz complexes at the DFT(PBE0)-optimized ground-state geometry. The bond dissociation energy (BDE) was obtained at the DFT(PBE0) level of theory, S_{LLCT} excitation energies (E) and electric transition dipole moments (μ_{el}) as well as ΔE_{ST} values of the LLCT states were computed with DFT/MRCI.

Carbene	E [eV]	ΔE_{ST}[meV]	μ_{el}[D]	Twist[a] angle[°]	C–M [pm]	M–N [pm]	BDE[b] [kJ mol^{-1}]
4NHC	3.92	139	4.07	2.0	186.3	185.9	262
4MAC	2.39	155	4.82	1.3	183.8	184.6	238
4CAAC(Ad)	3.39	174	3.56	0.2	186.1	186.2	279
4LAC(Ad)	2.44	185	4.76	2.8	183.7	185.0	258
5NHC	4.11	94	3.56	0.7	187.5	186.0	266
5MAC	3.28	115	3.54	0.0	187.0	185.4	255
5DAC	1.60	125	5.82	0.6	184.6	184.0	245
5CAAC(Ad)	3.45	163	3.34	6.7	188.9	187.4	273
5LAC(Ad)	2.53	161	4.25	1.9	186.9	186.1	259
6NHC	4.06	116	3.36	0.3	189.7	186.7	275
6MAC	3.20	108	3.44	2.5	188.7	186.1	258
6DAC	2.37	125	4.32	0.8	187.7	185.6	246
6CAAC(Me)	3.56	110	3.20	0.8	189.5	187.0	276
6CAAC(Ad)	3.25	98	2.61	28.9	192.3	189.8	246
6LAC(Me)	2.46	150	4.01	8.8	187.0	185.9	264
6LAC(Ad)	2.36	89	3.52	16.9	187.4	186.5	256

[a] N–C(carbene)–N(Cz)–C interligand dihedral angle.

[b] Difference between the electronic energies of the fully relaxed NHC-Cu-Cz complex and its fully relaxed (NHC/Cu–Cz) fragments. Zero-point vibrational energies and entropic contributions to the binding energy were not taken into account.

and DAC complexes. To this end, we built two-coordinate carbene–Cu–Cz complexes for all carbenes listed in table S1, optimized their electronic ground-state structures by means of DFT in the presence of a DCM solvent model and analyzed their vertical excitation spectra determined at the DFT/MRCI level of theory (figure 3 and table 1). In combination with typical energy lowerings of related CMA complexes upon relaxation of the excited-state geometry (about 0.5 eV for LLCT, 0.2 eV for MLCT and 0.15 eV for LC excited states) [13, 20], these vertical energies can be used to estimate adiabatic excitation energies of the relevant states. This computational approach has proven to be very successful in predicting and interpreting the spectral properties of transition metal carbene complexes [13, 19, 20, 55, 56].

In addition to LLCT and MLCT states, Cz ligand-centered (LC) states are found among the lowest-lying excited states in the Franck–Condon region. Because LLCT states promise to exhibit the smallest singlet–triplet energy splittings ΔE_{ST}, [19] we here focus on the energetics and spectral properties of their first LLCT states, even if these do not pose the lowest excited states at the ground-state equilibrium geometry. In addition to ΔE_{ST}, the electric dipole transition probability between the S_{LLCT} state and the electronic ground state is an interesting property to estimate the aptitude of a dye to serve as TADF emitter. In contrast to the oscillator strength, the electric transition dipole moment (μ_{el}) does not scale with the excitation energy, which is why we focus on this descriptor to compare the radiative properties of the carbene complexes.

In several papers dealing with design principles of CMA complexes [11, 16], the electron–hole density overlap and the distance between the electron and hole centroids are used as descriptors for estimating ΔE_{ST} and μ_{el}, respectively. Since our work aims to identify predictors for ΔE_{ST} and the radiative

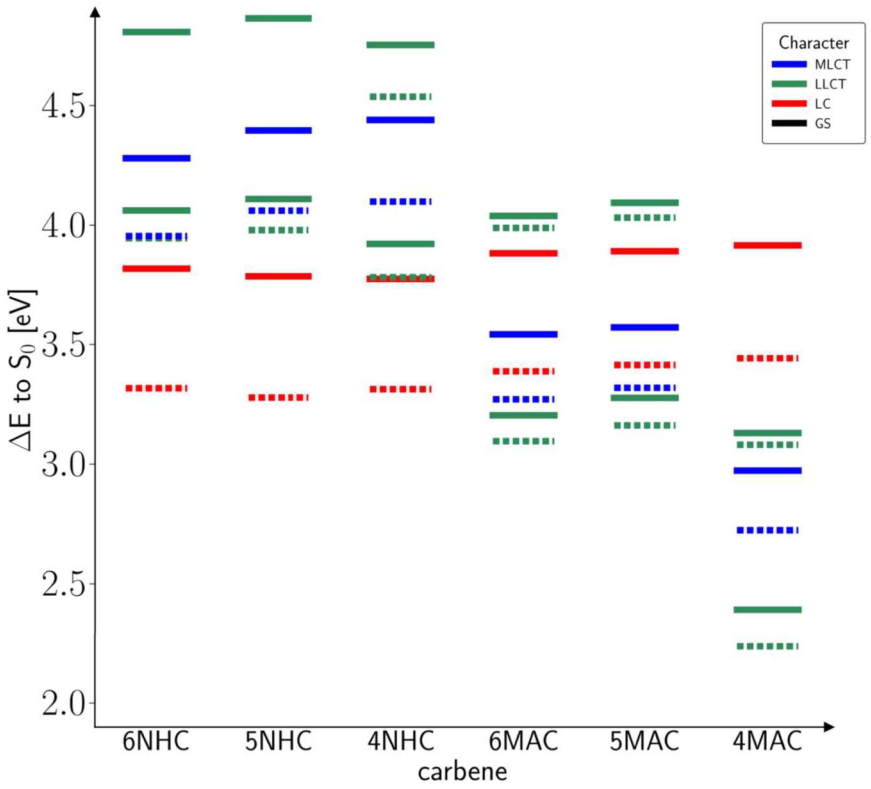

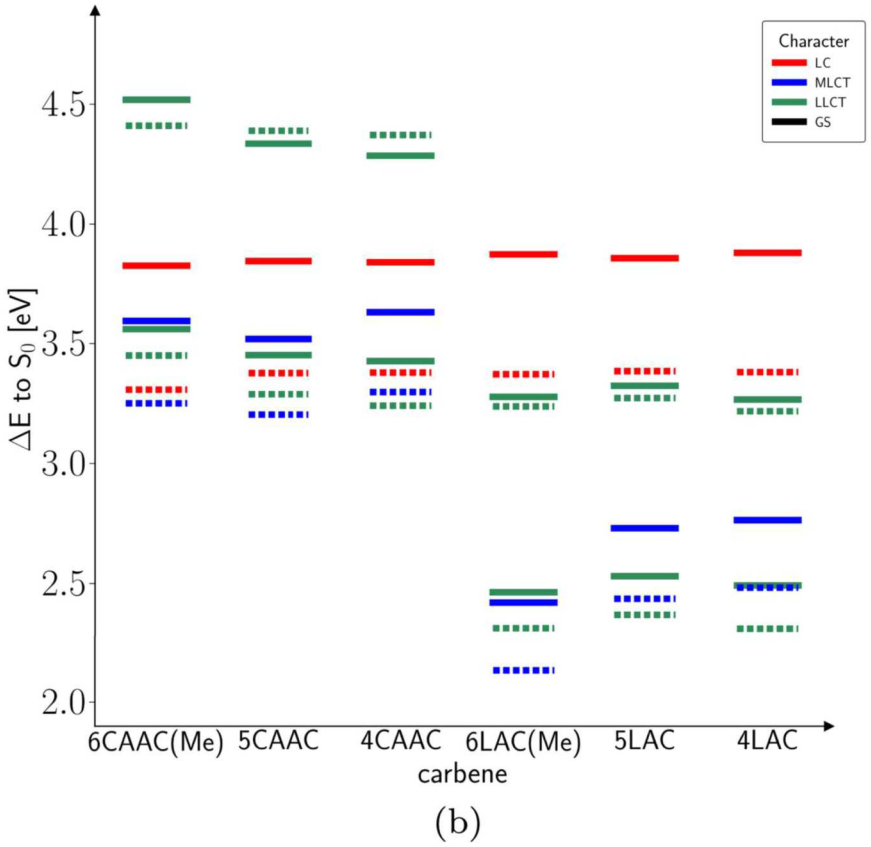

Figure 3. Vertical excitation energies for the (a) NHC- and MAC–Cu–Cz complexes and (b) CAAC- and LAC–Cu–Cz complexes at the optimized ground-state geometry. In the case of 6CAAC and 6LAC, the excitation energies of the corresponding 6CAAC(Me) and 6LAC(Me) complexes are shown. Solid lines denote singlet states, dashed lines denote triplet states. Next to the lowest three singlet and triplet excited states, the lowest LC(Cz) states and the second LLCT states are displayed.

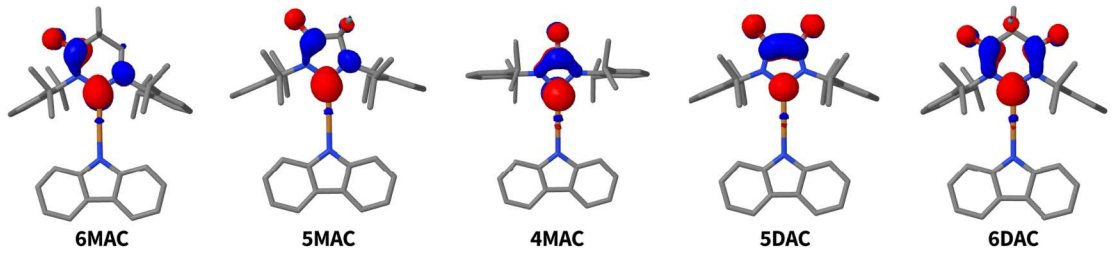

Figure 4. LUMOs of –Cu–Cz complexes with the respective carbenes. The isosurfaces were plotted for MO amplitudes of –0.05 (red) and +0.05 (blue).

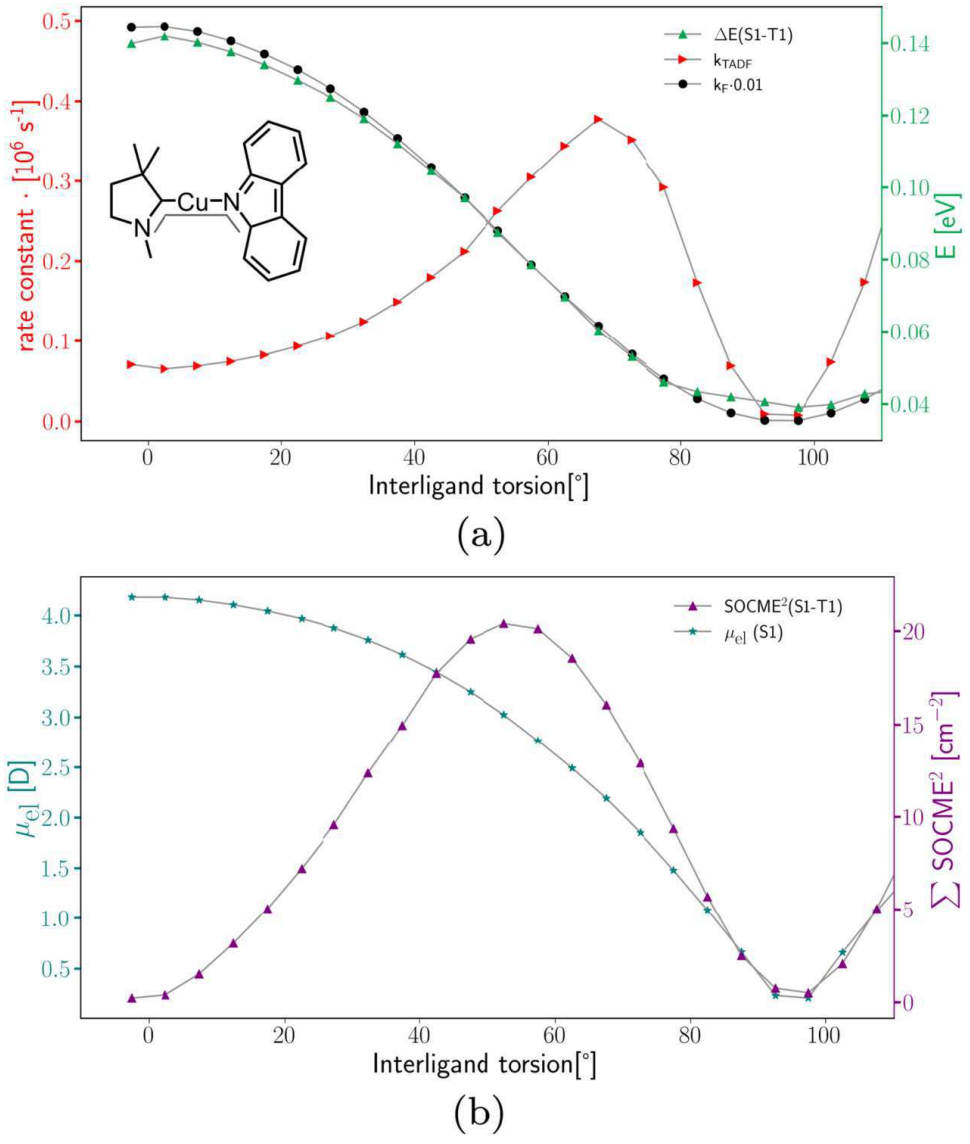

Figure 5. Photophysical properties of a sterically unhindered 5CAAC–Cu–Cz complex as functions of the interligand torsion angle. Geometries are from a constrained optimization in the electronic ground state. (a) ΔE_{ST} and estimated fluorescence rate constants. The population of the S_1 state relative to the T_1population [S] was calculated via a Boltzmann distribution at 298 K. k_{TADF} was obtained under the assumption of full S_1-T_1 equilibration via $k_{TADF}=[S] \cdot k_F$ neglecting other non-radiative decay channels. (b) Sum over squared SOCMEs of the S_1–T_1states as well as the electric transition dipole moment μ_{el} of the S_{LLCT}–S_0 transition.

transition probability from cost effective calculations, we tested the significance of these descriptors for our series of CMA complexes. Due to the lack of (good) correlation (for details see the Supplemental Data), we refrain from discussing these descriptors here, however.

In agreement with the moderate acceptor capabilities of the classical NHCs, we find the first

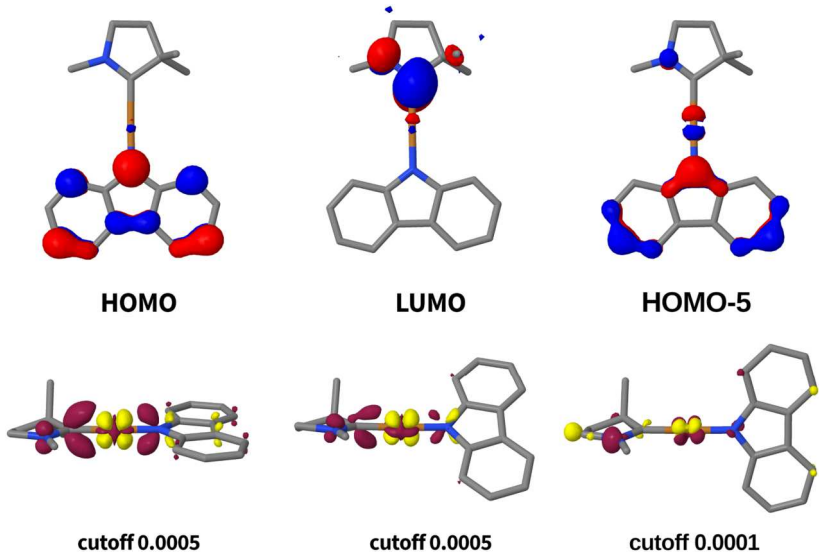

Figure 6. Top: Relevant orbitals for the S_1 and T_1 excitation of the complex displayed in figure 5(a) in a coplanar orientation of the ligands. The surfaces correspond to MO amplitudes with isovalues of –0.05 (red) and +0.05 (blue). Bottom: Difference of the T_{LLCT} and S_{LLCT} electron densities at constrained optimized geometries for a coplanar (left), diagonal (middle) and orthogonal (right) orientation of the ligands. Darkred-colored areas indicate a loss of electron density in the S_{LLCT} state, yellow-colored areas a gain. Here, the cutoff defines the fraction of the density outside the plotted isosurface.

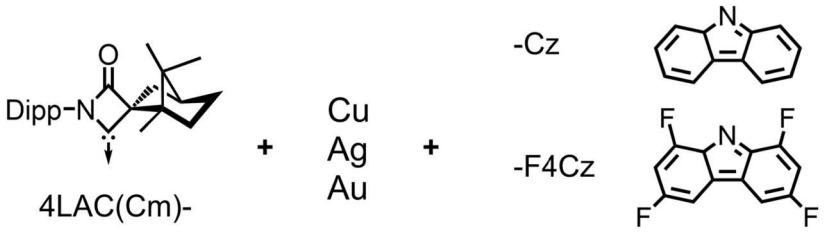

Figure 7. CMA complexes examined in detail.

S_{LLCT} state at vertical excitation energies of approximately 4 eV (figure 3(a) and table 1). Independent of the carbene ring size, a Cz ligand-centered (LC) $\pi\pi^*$ excitation forms the S_1 and T_1 states at the ground-state geometry. Here, the ^{3}LC state is located energetically at least 0.5 eV below the corresponding T_{LLCT} state. In view of the typical relaxation energies (see above), the ^{3}LC state is expected to form the lowest excited states of the NHC-complexes even adiabatically. Classical NHC complexes are therefore not further addressed in this work.

As discussed in section 3.1, the absence of a second neighboring nitrogen increases both, the acceptor and donor strengths of CAACs in comparison to classical NHCs. The change in the acceptor capabilities seems to prevail and stabilizes the LLCT states in the CAAC complexes in comparison to the corresponding NHC complexes (figure 3 and table 1). Many 5CAAC–M–Cz and some 6CAAC–M–Cz complexes are known as excellent TADF emitters in the solid state, in particular when the carbenes carry bulky substituents [1, 3–8]. Because the vertical energies of the lowest-lying states do not vary substantially with the size of the carbene ring (figure 3(b)) and table 1) and because the LLCT states are expected to form adiabatically the lowest excited singlet and triplet states, we predict 4CAAC–M–Cz complexes to possess good TADF properties as well.

The carbonyl group in the MAC and LAC backbones substantially increases the acceptor strength of the carbene and thus stabilizes the LLCT states w.r.t. the parent NHC- or CAAC-complex (figures 3(a) and (b)). We therefore expect that the emission wave length is further shifted into the red. Moreover, introduction of the electron-withdrawing C=O group in the backbone results in an increase of the μ_{el} value (table 1), an effect especially pronounced in the LAC complexes. For geometrical reasons (C=O bond aligned to C(carbene)–Cu–N(Cz) axis), the impact of the carbonyl group is largest for the 4MAC complex. Its properties more closely resembles those of the 5DAC and 6DAC complexes where the effect of the two carbonyl groups sum up to form a similar nodal structure of the LUMOs (figure 4). Interestingly, the MLCT states of the 6LAC complex are positioned at lower energies than their congeners in the 5LAC and 4LAC complexes (figure 3). The reversed energetic order of the T_{LLCT} and T_{MLCT} states in the Franck–

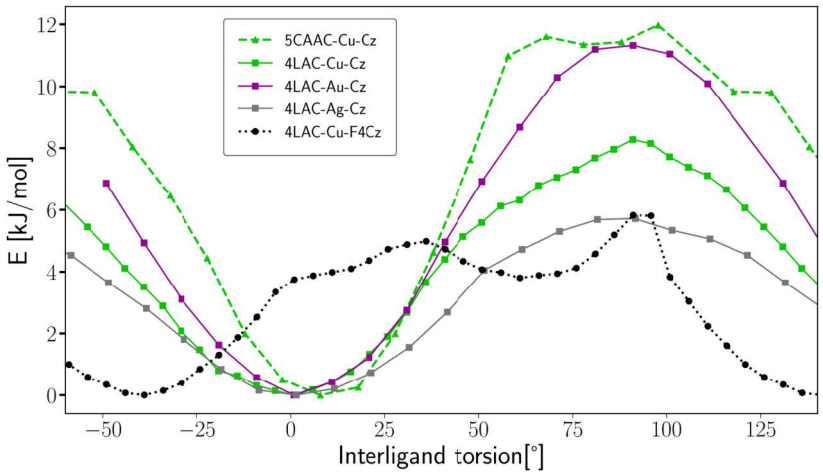

Figure 8. Relaxed PBE0 scan of the N–C(carbene)–N(Cz)–C torsion potential in the electronic ground states of selected complexes. The discontinuities of some lines are due to hysteresis.

Condon region might lead to phosphorescent 6LAC–Cu–Cz complexes. Due to the lower propensity of $Ag^{(I)}$ and $Au^{(I)}$ to form MLCT states, no such complication is expected for the 6LAC–Ag–Cz and 6LAC–Au–Cz complexes, however.

What effect does the ring size have in general? The S_{LLCT} excitation energy remains nearly constant within a given carbene class, save for 4MAC as discussed above. The singlet–triplet gap slightly decreases in the order $\Delta E_{ST}(4) > \Delta E_{ST}(5) > \Delta E_{ST}(6)$ (table 1). For a fixed type of carbene, we observe a steady increase of the electric transition dipole moment between the S_{LLCT} and the ground state with decreasing ring size. This property makes the 4MAC and 4LAC complexes interesting candidates for red-light or NIR emitting TADF compounds which is why we want to examine their properties in more detail.

With the exception of 6CAAC(Ad) and 6LAC(Ad), all minimum structures exhibit interligand dihedral angles N–C(carbene)–N(Cz)–C close to 0° (table 1). 6CAAC(Ad) and 6LAC(Ad) exhibit N–C(carbene)–C(spiro) angles of about 121° and 119°, respectively, and are therefore sterically too demanding to form complexes with approximately coplanar arrangements of the carbene and Cz ligands. With N–C(carbene)–C(spiro) angles of about 109° and 93°, respectively, in the corresponding five- and four-membered carbenes, the contact surface between the Ad residue and the Cz ligand is reduced and the tendency of the electronic ground state to form nearly coplanar conformers prevails. The impact of the interligand dihedral angle on the μ_{el} and ΔE_{ST} values is seen when the properties of the 6CAAC(Ad) and the sterically less demanding 6CAAC(Me) complexes are compared (table 1). The S_{LLCT} excitation energy is lowered, ΔE_{ST} shrinks and μ_{el} is markedly reduced.

A torsional scan on a sterically unhindered 5CAAC–Cu–Cz complex (figure 5) shows that a full twist of 90° yields minimal ΔE_{ST}, but is nevertheless unfavorable for the TADF properties as the μ_{el} value is minimal here. LMCT and MLCT admixture to the LLCT excitation is expected to aid the interstate SOC which is—besides a low ΔE_{ST} value—essential for efficient T_1–S_1 rISC. The course of the S_1–T_1 SOCMEs as function of the twist angle is less obvious than for μ_{el}, however. According to the extended El-Sayed rules [57–59], the d electrons and holes need to involve d orbitals with different orientations to ensure that the corresponding SOC integral is large. In a perfectly coplanar ligand alignment, both d_π contributors to the T_1–S_1 difference density lie in the same plane (figure 6, bottom left) and the mutual SOCME is small (figure 5(b)). A perpendicular ligand alignment does not automatically entail substantial S_1–T_1 SOCMEs, however. The reason is that the S_{LLCT} and T_{LLCT} wave functions have very similar compositions, save for the spin part, as visualized by a nearly vanishing S_{LLCT}–T_{LLCT} difference density (figure 6 bottom right). Because the SOC operator does not couple configurations with equal spatial occupations, conformers with perpendicular ligand alignments therefore feature small S_1-T_1 SOCMEs as well. In contrast, a partial twist of the ligand planes and hence of the d_π-type metal orbitals leads to sizeable SOC strengths. In the present example, a maximum of the SOC strength is found for a twist angle of about 45°. The course of k_{TADF} in figure 5(a), obtained under the assumption that non-radiative decay to the electronic ground state can be neglected, indicates that an interligand alignment between 60° and 75° can yield a three to four

Table 2. Properties of various carbene–M–Cz complexes at the DFT(PBE0)-optimized ground-state geometry of the most stable conformer. Torsional barrier heights (TBH) and backbonding strengths (BBS) were obtained at the DFT (PBE0) level of theory, vertical S_{LLCT} excitation energies E, electric transition dipole moments (μ_{el}) and absorption oscillator strengths f as well as ΔE_{ST} values were computed with DFT/MRCI.

Complex	E [eV]	ΔE_{ST} [meV]	μ_{el} [D]	f	Twist [°]	C–M [pm]	M–N [pm]	TBH [kJ mol^{-1}]	BBS [kJ mol^{-1}]
5CAAC(Ad)–Cu–Cz	3.45	163	3.34	0.146	6.7	189	187	12.0	41.8
4LAC(Cm)–Cu–Cz	2.49	180	4.70	0.209	−5.2	184	185	8.3	59.2
4LAC(Cm)–Ag–Cz	2.58	63	3.48	0.118	10.6	204	206	5.7	41.7
4LAC(Cm)–Au–Cz	2.64	131	5.28	0.278	0.4	195	202	11.3	91.8
4LAC(Cm)–Cu–4FCz	2.70	111	3.56	0.130	−44.5	184	187	5.8	58.9
4LAC(Cm)–Ag–4FCz	2.86	47	2.94	0.094	−50.1	203	207	3.3	42.0
4LAC(Cm)–Au–4FCz	2.86	119	5.12	0.285	−48.1	194	203	7.9	93.8

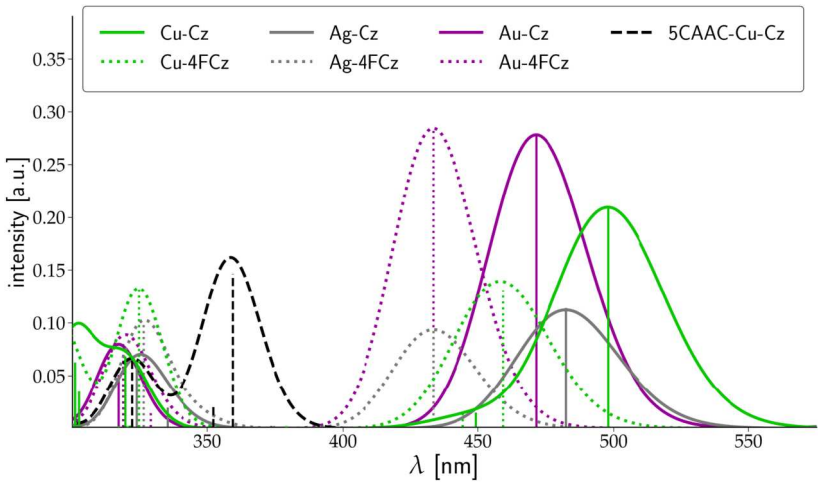

Figure 9. Computed ground-state absorption spectra of 4LAC(Cm) complexes. The line spectra were broadened by Gaussians with 1895 cm^{-1} full width at half maximum. All complexes exhibit coplanar ground state minima.

times higher TADF rate constant compared to a coplanar conformer.

3.3. Detailed investigation of the photophysical properties of 4LAC complexes

As reported in earlier work by some of us, free 4MACs tend to dimerize in situ upon their formation [17]. In contrast, rhodium and iridium complexes of 4LACs could be prepared and characterized [18]. This prompted us to investigate a 4LAC–coinage metal–Cz triad (figure 7) in more detail and to compare its properties with the well-known 5CAAC(Ad)–Cu–Cz complex. To induce a twist of the amide ligand, we opted for a bulky but highly asymmetric spiro-fused alkane, a camphore-derived bicyclo[2.2.1]heptane (Cm), instead of an adamantane residue.

3.3.1. Ground-state conformers and absorption properties

We examined the impact of the carbene and the coinage metal ions on the conformation by computing torsion profiles around the C(carbene)–M–N(Cz) axis (figure 8). Despite the steric demand of the carbene ligand, the torsion profiles of all Cz complexes exhibit a minimum at approximately 0° and a maximum close to 90°, showing that this is not the decisive property directing the carbene–Cz alignment. Rather, we find a correlation between the strength of the M–carbene π-type backbond within the Cu, Ag, Au triad and the height of the torsion barrier which increases in the order Ag < Cu < Au although the metal bonds are markedly longer in the Au complex than in its Cu congener (table 2). The larger N–C(carbene)–C(spiro) angle in the five-membered carbene ring increases the steric demand of 5CAAC(Ad) in comparison to 4LAC (Cm) and elongates the C–M bond. As expected, the torsion barrier is higher for the five-membered carbene Cu(I) complex and the torsion profile narrower in comparison to the respective complex with 4LAC(Cm). Nevertheless, as long as Cz is used as the donor ligand, all complexes exhibit torsion barrier heights below 12 kJ mol^{-1}, sufficiently low to be overcome at room temperature in solution.

Comparing the spectroscopic properties of 4LAC (Cm)–Cu–Cz in the FC region with those of its well-known 5CAAC(Ad)–Cu–Cz relative, it is seen that the S_{LLCT} excitation energy is reduced by about 1 eV in the 4LAC complex (table 2). Despite the red-shift, the oscillator strength of the S_{LLCT} transition is higher in 4LAC(Cm)–Cu–Cz. When $Cu^{(I)}$ is replaced by $Ag^{(I)}$, the S_{LLCT} absorption is slightly blue-shifted. The lower participation of the metal to the excitations (table S2) causes the silver complexes to have the smallest ΔE_{ST} values and oscillator strengths among the 4LAC(Cm)–M–Cz complexes. Like in many other two-coordinate coinage metal complexes, the intensity of the absorption increases in the order Ag < Cu < Au (figure 9).

Due to the lower buried volume of four-membered carbenes in comparison to their five-membered congeners (table S1), it is difficult to foresee the impact of sterically demanding Cz derivatives on the equilibrium interligand torsion angle of the 4LAC(Cm) complexes. Methylation of Cz in 1- and 8-positions positions leads to ligand twists with minima in the desired range of about –60° or 120°. However, the twist goes along with a marked tilt of the Cz ligand plane in coplanar ligand orientations (figure S4) which is expected to promote the nonradiative deactivation of the complex. We have therefore refrained from investigating the properties of this complex in more detail. Instead, we studied 4LAC(Cm)–M–4FCz complexes carrying fluorine atoms in 1, 3, 6, and 8 positions (figure S5). For the most

Table 3. Room temperature TADF properties of 4LAC(Cm) complexes undergoing constrained geometry optimization in the S_{LLCT} and T_{LLCT} states.

Complex	Twist[a] Angle[°]	ΔE_{ST}[b] [meV]	μ_{el}[D]	k_F [s^{-1}]	k_{rISC} [s^{-1}]	k_{ISC} [s^{-1}]	k_{TADF}[c] [s^{-1}]	λ_F [nm]
4LAC(Cm)–Cu–Cz	−5.2	169	4.630	2.48×10^{07}	6.35×10^{06}	1.18×10^{09}	1.31×10^{05}	647
4LAC(Cm)–Ag–Cz	10.6	25	3.627	1.34×10^{07}	5.61×10^{08}	2.57×10^{09}	2.93×10^{06}	675
4LAC(Cm)–Au–Cz	0.4	105	5.272	3.75×10^{07}	2.41×10^{07}	4.20×10^{08}	2.06×10^{06}	615
4LAC(Cm)–Cu–4FCz	−44.5	112	3.606	1.86×10^{07}	1.04×10^{09}	2.21×10^{10}	8.63×10^{05}	603
4LAC(Cm)–Ag–4FCz	−50.1	37	2.861	1.05×10^{07}	5.67×10^{08}	2.17×10^{09}	2.74×10^{06}	626
4LAC(Cm)–Au–4FCz	−48.1	84	4.276	2.42×10^{07}	1.86×10^{10}	1.82×10^{11}	2.56×10^{06}	590

[a] The N–C(arbene)–N(Cz)–C interligand dihedral angle was fixed to its value at the ground-state minimum during the constrained excited-state optimization.

[b] Adiabatic S_{LLCT}-T_{LLCT} energy difference.

[c] Calculated according to $k_{TADF} = k_{rISC} \times \left(1 - \frac{k_{ISC}}{k_F + k_{ISC}}\right)$ [3].

Table 4. Excited-state properties of the 4LAC–Au–Cz and 4LAC–Au–4FCz complexes computed at optimized geometries of the T_{LLCT} state.

Property	Donor	Ligand–ligand alignment		
		coplanar[a] (0.44°)	diagonal[b] (48°)	orthogonal (83-87°)
$\sum SOCME^2$ (S_1-T_1)	Cz	8.30	324.00	11.85
	4FCz	7.56	453.40	15.20
μ_{El} [D]	Cz	6.063	4.554	0.078
	4FCz	6.256	4.733	0.114

[a] For 4FCz, a frozen structure of Cz congener was used with H replaced by F and F–C bond lengths relaxed.

[b] Diagonal structures of the Cz ligand were obtained via constrained optimization of the T_{LLCT} geometry.

stable conformer, twist angles between –45° and –50° are obtained (table 2). Interestingly, the torsion barrier height of 4LAC(Cm)–Cu–4FCz is smaller than for the parent 4LAC(Cm)–Cu–Cz complex (figure 8). We ascribe this reduction at torsional angles close to coplanar ligand alignments to steric repulsion which mitigates the directional effect of the metal-to-ligand backbond.

To the best of our knowledge, previous attempts to obtain such a 60–75°donor–acceptor twist in CMA complexes without tilting the donor have been unsuccessful. Substitution of hydrogen by fluorine in the 1- and 8-positions of Cz in 5CAAC(Ad)–Au–Cz yielded crystal structures with a barely changed interligand twist and tilt whereas crystal structures with a >80° twist were found in the corresponding $Cu^{(I)}$ complex [24]. In contrast, methylation of Cz in 1- and 8-positions led to crystal structures of two-coordinate gold and copper complexes with nearly orthogonal alignment of the 5CAAC and 1,8-dimethylcarbazolyl (or 1,3,6,8-tetramethylcarbazolyl) ligands and markedly increased nonradiative decay [4, 24].

3.3.2. TADF properties of the 4LAC(Cm)–M–Cz complexes

The lowest-lying LLCT states experience large energetic stabilization upon geometry relaxation and any obvious energetic proximity to MLCT or LC states is lifted (figures S6–S12). This allows us to focus on the S_{LLCT} and T_{LLCT} states for the description of their TADF behavior. Note, however, that their wave functions still contain varying amounts of LMCT and MLCT contributions (tables S2 and S3). The MLCT admixtures are particulary pronounced in the T_{LLCT} state of the copper complex. As we will see below, these metal contributions have considerable impact on the ΔE_{ST} values and the mutual S_{LLCT}–T_{LLCT} SOCMEs.

The LLCT excited states of the 4LAC(Cm)–M–Cz complexes possess global minima at orthogonal ligand alignments (table S7). Here, the Coulomb repulsion and the exchange interaction of the electrons in the frontier orbitals are lowest. Because the ΔE_{ST} value is proportional to the magnitude of the exchange interaction, it is maximal at coplanar ligand alignments. The singlet–triplet energy splitting thus reinforces the tendency of the S_{LLCT} state towards orthogonal ligand alignments whereas it counteracts this tendency in the T_{LLCT} case. Steric influences can overrule the electronic preferences, however. A crystal environment, for example, can prevent a full geometry relaxation of the CMAs in the solid state. In particular, the large-amplitude twist of the donor ligand is sterically hindered and the donor ligand
will librate about its equilibrium position in the electronic ground state [20]. To model the photophysical behavior of 4LAC(Cm)–M–Cz in a rigid environment, we therefore resorted to constrained geometry optimizations for the LLCT states, fixing the interligand dihedral angle to its value in the ground-state minimum.[3]

The good acceptor properties of the 4LAC(Cm) carbene result in bright S_{LLCT} states with k_F values above $10^7\ s^{-1}$ and emission in the deep red region of the visible spectrum (table 3). ISC outcompetes the fluorescence by at least an order of magnitude. We therefore expect prompt fluorescence to decay rapidly. The small metal participation in the LLCT states of the silver complex (tables S2 and S3) causes a minute ΔE_{ST} of 25 meV and leads to the highest rISC rate constant in the coinage metal series. In contrast, the large MLCT admixture to the LLCT excited states of the copper complex gives rise to a ΔE_{ST} splitting of 169 meV, a relatively high value for LLCT states in CMAs. It causes the rISC rate to be much smaller than the ISC rate. The rISC processes of all other complexes are, however, fast enough to achieve rapid equilibration of the S_1-T_1 populations. Internal conversion rates are difficult to compute reliably. However, in related CAArC- and DAC–Cu–Cz complexes emitting in the deep red as well, nonradiative decay rates k_{nr} in the order of $10^6\ s^{-1}$ were reported in the solid state [13, 14]. Under these premises, the 4LAC–Ag–Cz and 4LAC–Au–Cz complexes are predicted to possess sub-μs TADF decay, mostly owing to their large fluorescence rate constants. The quantum yield of TADF in the corresponding 4LAC–Cu–Cz complex is considered to be mainly limited by a low rISC/ISC ratio due to a suboptimal ΔE_{ST}.

[3] Strictly, the Condon approximation of the radiative and nonradiative transition probabilities is not valid in such floppy molecules where even small variations of the energy can affect large-amplitude motions [60]. However, modeling non-Condon effects is extremely resource intensive and performed mostly in cases where transition probabilties are small. Because the fluorescence rate constants and the rISC/ISC ratios of the here investigated complexes are already very high in Condon approximation, we do not expect a substantial qualitative impact of the non-Condon effects on the TADF kinetics.

3.3.3. TADF properties of the 4FCz complexes

The fluorinated 4LAC complexes possess smaller $\mu_{el}(S_{LLCT})$ values than their unfluorinated counterparts. The reduction is mainly brought about by the interligand twist and is not predominantly caused by electronic effects. To see this, we constructed a diagonal T_{LLCT} structure of the 4LAC(Cm)–Au–Cz and a coplanar one of the 4LAC(Cm)–Au–4FCz. For a fixed twist angle, the $\mu_{el}(S_{LLCT})$ values of the fluorinated and unfluorinated Cz-complexes are similar (table 4).

The slight decrease of the radiative rate constant is overcompensated, however, by better TADF properties. Like in the 5CAAC–Cu–Cz complex (figure 5), the ΔE_{ST} value steadily decreases with increasing interligand twist angle in the 4LAC–Au–Cz and 4LAC–Au–4FCz complexes and the mutual SOC between S_{LLCT} and T_{LLCT} is maximal at diagonal alignments of the ligands (table 4). The similarity between the SOCMEs of the Cz and 4FCz complexes at a given twist angle suggests that even in this case the predominant impact of the fluorine atoms does not have an electronic origin but stems from the different ligand–ligand orientation it induces. Due to the reduced ΔE_{ST} and higher SOCMEs, the 4LAC–Cu–4FCz and 4LAC–Au–4FCz complexes exhibit substantially larger rISC rate constants and better k_{ISC} to k_{rISC} ratios than the related Cz complexes (table 3). Interestingly, the predicted TADF properties of the 4LAC–Ag–Cz complex, which showed the highest rISC rate constant in the coinage metal series, are nearly unchanged upon fluorination, save for a blue-shift of the emission wave length.

4. Conclusion

In summary, the results of our computational study suggest that the lactam-based four-membered carbene 4LAC, carrying a bulky Dipp substituent at the nitrogen atom and a spiro-fused bicyclic heptane substituent adjacent to the carbene site, is apt to form two-coordinated carbene metal amides with excellent TADF properties in the solid state. The 4LAC–M–Cz (M = $Cu^{(I)}$, $Ag^{(I)}$ and $Au^{(I)}$, Cz = carbazolide) complexes possess ground-state structures with nearly coplanar orientation of the ligands and binding energies comparable to those of five- und six-membered MACs and LACs. The small metal participation in the first excited LLCT states of the silver complex causes a minute ΔE_{ST} value of merely 25 meV and leads to the highest rISC rate constant ($6 \times 10^8\ s^{-1}$) in the coinage metal series. In combination with the large electric transition dipole moments of the S_{LLCT} state in coplanar ligand arrangements, submicrosecond radiative decay of the red-light emission is predicted for this complex in the solid state. The high admixture of MLCT character into S_1 and T_1 wave functions of the copper complex results in a comparably large singlet–triplet splitting and a lower rISC rate constant ($6 \times 10^6\ s^{-1}$) despite substantial SOC. The TADF performance of the gold complex is similar to the one of the silver complex because its higher ΔE_{ST} value is mitigated by an increased fluorescence rate constant.

One way to reduce the singlet–triplet energy gap in linear donor–acceptor compounds is a twist about the connecting bond(s), thus decoupling donor and acceptor moieties electronically. Full geometry relaxation of the 4LAC–M–Cz complexes in the S_{LLCT} state leads to an almost perpendicluar arrangement of the ligands with minimal ΔE_{ST} value. However, the electric dipole transition moment μ_{el} vanishes here as well, while SOC is still efficient. We may therefore assume that the fluorescence of the sterically unhindered 4LAC–M–Cz complexes is quenched or at least very weak in liquid solution.

To bring about a moderate ligand twist while avoiding a perpendiculer ligand alignment, we introduced substituents in the 1 and 8 positions of the Cz donor. Methylation in these positions led to an additional tilt of Cz plane which is known to promote nonradiative deactivation, but fluorination in 1, 3, 6, and 8 positions yielded the desired effect. The fluorinated 4LAC complexes have ground-state equilibrium structures in which the 4FCz ligands are twisted by 45 to 50° w.r.t. the plane of the four-membered carbene ring. While these twist angles do not quite fall in the optimal range (60–75°) for TADF activity, as determined for a related 5CAAC–Cu–Cz complex, they are sufficiently large to enhance the TADF properties of the 4LAC–Cu–Cz and 4LAC–Au–Cz complexes. The electronic decoupling of the donor and acceptor moieties upon torsion goes along with a moderate reduction of the transition dipole strength and a blue shift of the S_{LLCT} emission. With regard to their TADF properties, the reduction of the fluorescence rate constant is overcompensated in the $Cu^{(I)}$ and $Au^{(I)}$ complexes, however, by a decrease of the ΔE_{ST} value, thus improving the k_{rISC} to k_{ISC} ratios and TADF rate constants. Moreover, with k_{rISC} values of the order of $10^9\ s^{-1}$ ($Cu^{(I)}$ complex) and $10^{10}\ s^{-1}$ ($Au^{(I)}$ complex), the rISC process should have a competitive advantage over common triplet deactivation processes such as triplet–triplet annihilation.

Acknowledgments

The authors have declared that no conflicting interests exist.

Data availability statement

All data that support the findings of this study are included within the article (and any supplementary files).

Funding

The authors thank the Deutsche Forschungsgemeinschaft (DFG, German Research Foundation) for financial support through GRK 2482, project number 396890929.

Author contributions

Jasper Guhl 0000-0001-5075-0158
Conceptualization (lead), Investigation (lead), Visualization (lead), Writing – original draft (supporting)

Tu Viet Chu
Investigation (supporting)

Tobias Kretschmer 0009-0004-1277-8650
Investigation (supporting)

Leonard Karl 0000-0002-7129-4080
Conceptualization (supporting)

Christian Ganter 0000-0003-0567-5982
Conceptualization (supporting), Funding acquisition (equal), Supervision (equal), Writing – original draft (supporting)

Christel M Marian 0000-0001-7148-0900
Conceptualization (supporting), Funding acquisition (equal), Supervision (equal), Writing – original draft (lead)

References

[1] Di D *et al* 2017 *Science* **356** 159–63
[2] Romanov A S, Jones S T E, Yang L, Conaghan P J, Di D, Linnolahti M, Credgington D and Bochmann M 2018 *Adv. Opt. Mater.* **6** 1801347
[3] Hamze R *et al* 2019 *J. Am. Chem. Soc.* **141** 8616–26
[4] Hamze R *et al* 2019 *Science* **363** 601–6
[5] Chotard F, Sivchik V, Linnolahti M, Bochmann M and Romanov A S 2020 *Chem. Mater.* **32** 6114–22
[6] Romanov A *et al* 2020 *Chem. Sci.* **11** 435–46
[7] Conaghan P J, Matthews C S B, Chotard F, Jones S T E, Greenham N C, Bochmann M, Credgington D and Romanov A S 2020 *Nat. Comm.* **11** 1758
[8] Jazzar R, Soleilhavoup M and Bertrand G 2020 *Chem. Rev.* **120** 4141–68
[9] Hossain J, Akhtar R and Khan S 2021 *Polyhedron* **201** 115151
[10] Reponen A P M, Chotard F, Lempelto A, Shekhovtsev V, Credgington D, Bochmann M, Linnolahti M, Greenham N C and Romanov A S 2022 *Adv. Opt. Mater.* **10** 2200312
[11] Phuoc N L, Brannan A C, Romanov A S and Linnolahti M 2023 *Molecules* **28** 4398
[12] Riley C, Jones W, Phuoc N L, Linnolahti M and Romanov A S 2025 *Org. Electron.* **137** 107156
[13] Gernert M, Balles-Wolf L, Kerner F, Müller U, Schmiedel A, Holzapfel M, Marian C M, Pflaum J, Lambert C and Steffen A 2020 *J. Am. Chem. Soc.* **142** 8897–909
[14] Shi S, Jung M C, Coburn C, Tadle A, Sylvinson M R D, Djurovich P I, Forrest S R and Thompson M E 2019 *J. Am. Chem. Soc.* **141** 3576–88
[15] Hamze R, Idris M, Muthiah Ravinson D S, Jung M C, Haiges R, Djurovich P I and Thompson M E 2020 *Front. Chem.* **8** 401
[16] Avula S, Jhun B H, Jo U, Heo S, Lee J Y and You Y 2024 *Adv. Sci.* **11** 2305745
[17] Karl L, Meisner J and Ganter C 2023 *Eur. J. Inorg. Chem.* **26** e202300022
[18] Karl L, Deißenbeck D, Meisner J and Ganter C 2025 *Chem. Eur. J* **31** e202501320
[19] Lüdtke N, Föller J and Marian C M 2020 *Phys. Chem. Chem. Phys.* **22** 23530–44
[20] Föller J and Marian C M 2017 *J. Phys. Chem. Lett.* **8** 5643–7
[21] Thompson S, Eng J and Penfold T J 2018 *J. Chem. Phys.* **149** 014304
[22] Hall C R, Romanov A S, Bochmann M and Meech S R 2018 *J. Phys. Chem. Lett.* **9** 5873–6
[23] Eng J, Thompson S, Goodwin H, Credgington D and Penfold T J 2020 *Phys. Chem. Chem. Phys.* **22** 4659–67
[24] Gu Q, Chotard F, Eng J, Reponen A P M, Vitorica-Yrezabal I J, Woodward A W, Penfold T J, Credgington D, Bochmann M and Romanov A S 2022 *Chem. Mater.* **34** 7526–42
[25] Cances E, Mennucci B and Tomasi J 1997 *J. Chem. Phys.* **107** 3032–41
[26] Cammi R, Corni S, Mennucci B and Tomasi J 2005 *J. Chem. Phys.* **122** 104513
[27] Scalmani G, Frisch M J, Mennucci B, Tomasi J, Cammi R and Barone V 2006 *J. Chem. Phys.* **124** 94107
[28] Frisch M J *et al* 2016 *Gaussian 16 Revision C.01* (Gaussian Inc.)
[29] Perdew J P, Burke K and Ernzerhof M 1996 *Phys. Rev. Lett.* **77** 3865–8
[30] Adamo C and Barone V 1999 *J. Chem. Phys.* **110** 6158–70
[31] Weigend F and Ahlrichs R 2005 *Phys. Chem. Chem. Phys.* **7** 3297–305
[32] Andrae D, Häußermann U, Dolg M, Stoll H and Preuß H 1990 *Theor. Chim. Acta* **77** 123–41
[33] Peterson K A and Puzzarini C 2005 *Theor. Chem. Acc.* **114** 283–96
[34] Figgen D, Rauhut G, Dolg M and Stoll H 2005 *Chem. Phys.* **311** 227–44
[35] Runge E and Gross E K U 1984 *Phys. Rev. Lett.* **52** 997–1000
[36] Furche F and Ahlrichs R 2002 *J. Chem. Phys.* **117** 7433–47
[37] Hirata S and Head-Gordon M 1999 *Chem. Phys. Lett.* **314** 291–9
[38] Reed A E, Curtiss L A and Weinhold F 1988 *Chem. Rev.* **88** 899–926
[39] Grimme S and Waletzke M 1999 *J. Chem. Phys.* **111** 5645–55
[40] Marian C M, Heil A and Kleinschmidt M 2019 *WIREs Comput. Mol. Sci.* **9** e1394
[41] Becke A D 1993 *J. Chem. Phys.* **98** 1372–7
[42] Lee C, Yang W and Parr R G 1988 *Phys. Rev. B* **37** 785–9
[43] Weigend F, Häser M, Patzelt H and Ahlrichs R 1998 *Chem. Phys. Lett.* **294** 143–52
[44] TURBOMOLE V7.5.0 2020, a development of University of Karlsruhe and Forschungszentrum Karlsruhe GmbH, 1989-2007, TURBOMOLE GmbH, since 2007; available from http://www.turbomole.com
[45] Plasser F 2020 *J. Chem. Phys.* **152** 084108
[46] Jmol: an open-source java viewer for chemical structures in 3d. http://www.jmol.org/
[47] Kleinschmidt M, Tatchen J and Marian C M 2002 *J. Comput. Chem.* **23** 824–33
[48] Kleinschmidt M and Marian C M 2005 *Chem. Phys.* **311** 71–9
[49] Kleinschmidt M, van Wüllen C and Marian C M 2015 *J. Chem. Phys.* **142** 094301
[50] Heß B A, Marian C M, Wahlgren U and Gropen O 1996 *Chem. Phys. Lett.* **251** 365–71

[51] Etinski M, Tatchen J and Marian C M 2011 *J. Chem. Phys* **134** 154105
[52] Etinski M, Tatchen J and Marian C M 2014 *Phys. Chem. Chem. Phys.* **16** 4740–51
[53] Böhmer T, Kleinschmidt M and Marian C M 2024 *J. Chem. Phys.* **161** 094114
[54] Kleinschmidt M, Tatchen J and Marian C M 2006 *J. Chem. Phys.* **124** 124101
[55] Mitra M, Mrózek O, Putscher M, Guhl J, Hupp B, Belyaev A, Marian C M and Steffen A 2024 *Angew. Chem. Intl. Ed.* **63** e202316300
[56] Guhl J, Sretenović D, Schmeinck P, Felekyan S, Kühnemuth R, Ganter C, Seidel C A M, Marian C M and Suta M 2024 *J. Mater. Chem. C* **12** 10036–52
[57] Marian C M 2021 *Annu. Rev. Phys. Chem.* **72** 617–40
[58] Capano G, Rothlisberger U, Tavernelli I and Penfold T J 2015 *J. Phys. Chem. A* **119** 7026–37
[59] Steffen A and Hupp B 2021 Design of efficient emissive materials *Comprehensive Coordination Chemistry* 3rd ed E C Constable *et al* (Elsevier) pp 466–502
[60] Penfold T J, Gindensperger E, Daniel C and Marian C M 2018 *Chem. Rev.* **118** 6975–7025